Theoretical and Applied Fracture Mechanics 104 (2019) 102380

Contents lists available at ScienceDirect

Theoretical and Applied Fracture Mechanics

journal homepage: www.elsevier.com/locate/tafmec

Use of local approaches to calculate changes in cleavage fracture toughness due to pre-straining and constraint effects

Andrey P. Jivkov[a,*], Diego Sarzosa Burgos[b], Claudio Ruggieri[b], Jack Beswick[c], Rafael Savioli[b], Peter James[c], Andrew Sherry[d]

[a] Mechanics and Physics of Solids Research Group, School of MACE, The University of Manchester, Oxford Road, Manchester M13 9PL, UK
[b] Department of Naval Architecture and Ocean Engineering, University of Sao Paulo, Sao Paulo, Brazil
[c] Wood, Birchwood Park, Warrington WA3 6AE, UK
[d] National Nuclear Laboratory, Birchwood Park, Warrington WA3 6AE, UK

ARTICLE INFO

Keywords:
Ferritic steels
Cleavage fracture
Load history
Shallow cracks
Apparent toughness
Local approach

ABSTRACT

Presented are experimental data and analyses of fracture toughness tests across three different crack tip constraint conditions and two different material conditions – as-received and pre-strained to 5% plastic strain. Analyses are performed using a local approach, based on a plasticity-modified Weibull stress interpreted as a crack driving force for cleavage fracture. Local approach parameters are calibrated using experimental data from the highest and lowest constraint geometries of as-received material. Results suggest one point of practical importance for testing reduction: use of large constraint difference for calibration yields good predictions for cleavage fracture toughness at intermediate constraints; use of small constraint difference for calibration cannot guarantee good predictions for constraints outside the calibration interval. Further, the calibrated local approach is used to predict the fracture toughness of pre-strained material. Pre-straining is found to reduce both the elastic modulus and the proportionality stress of the material, which at the micro-structural scale could be attributed to increased dislocation mobility after unpinning, and in addition to possible damage around second phase particles. Resulting characteristic toughness values are 2–2.5 times smaller than those of as-received material for corresponding constraint conditions, with pronounced diminishing constraint benefit. The degradation of deformation properties changes the initial conditions for Weibull stress calculation. A simple scaling method is proposed, based on flow stress changes, to account for changes in initial conditions. Predictions based on the proposed Weibull stress scaling are shown to be in good agreement with experimental data. This suggests a second point of practical importance for testing reduction: changes in fracture toughness due to load history could be predicted using only tensile test data of aged material and tensile and fracture toughness data from original material at two significantly different constraint conditions. Further experimental evidence is required to support this suggestion.

1. Introduction

Ferritic steels are widely used for fabrication of pressure boundary elements, such as pipes and vessels, due to their high strength and good ductility [1]. They exhibit cleavage fracture at sufficiently low temperatures [2], which might not be a concern at the start of component service, but could become critical due to service-related material degradation, e.g. irradiation embrittlement of nuclear reactor vessels [3], or hydrogen embrittlement of oil and gas pipes [4]. In addition, the propensity for cleavage fracture could be enhanced by the presence of residual stresses, e.g. around welds [5], as well as by pre-service plastic strains introduced in weld heat affected zones or during proof testing of the equipment [6]. While the integrity assessment using pre-fabrication materials' properties is a well-established process, the role of residual stresses and initial plastic strains is not sufficiently understood. This is reflected in the conservatism of the existing assessment procedures.

One aim of this work is to demonstrate that existing local approaches to fracture can be used to infer the change of material fracture toughness due to pre-service plastic strains from knowledge of the change of deformation properties. This means that only standard tensile tests of a material with different levels of plastic pre-strain will be sufficient in order to determine the corresponding changes of the cleavage fracture toughness. A second aim is to show that with a calibration of local approach parameters between high and very low

* Corresponding author.
E-mail address: andrey.jivkov@manchester.ac.uk (A.P. Jivkov).

https://doi.org/10.1016/j.tafmec.2019.102380
Received 27 February 2019; Received in revised form 25 September 2019; Accepted 30 September 2019
Available online 13 October 2019

constraint geometries, the fracture toughness across the whole interval of constraint conditions can be calculated for virgin as well as for pre-strained materials.

Section 2 contains a brief review of the mathematical basis and the assumptions behind the local approaches to cleavage fracture. Section 3 gives a description of a test programme including tensile and fracture toughness tests with three different crack tip constraints and two material states – as received and uniformly pre-strained to 5% plastic strain. Details of the corresponding finite element modelling and the application of local approaches are given in Section 4. Results are presented and discussed in Section 5. The paper finishes with conclusions and perspectives for advancement of the local approaches.

2. Experimental and theoretical bases of local approaches to cleavage

2.1. Probability of cleavage fracture

Cleavage is characterized by unstable propagation of a crack typically originating from a ruptured second-phase particle, such as metal carbide or sulphate [7]. Second-phase particles are elastic-brittle and break due to raising internal stresses as they accommodate the total strains of the plastically deforming surroundings, a process referred to as the plastic overload [8]. A characteristic feature of the cleavage fracture phenomenon is its statistical nature, i.e. the experimentally measured toughness values at a given temperature show a significant scatter [9]. This arises from the spatially random distribution of second-phase particles of variable sizes, which might be converted into micro-cracks of variable sizes by plastic overload.

It should be noted that, depending on the local mechanical fields, a particle of given size may: (1) remain intact, i.e. continue deforming with the matrix; (2) detach from the matrix forming a void, which grows with further plastic straining; (3) break, forming a micro-crack which blunts due to local conditions and continues as in (2); and (4) break, forming a micro-crack which can propagate to cleave the component. Thus, we distinguish between particles, voids/micro-cracks not eligible for cleavage initiation, and micro-cracks eligible for cleavage.

If $f_c(a)$ denotes the probability density of eligible micro-crack sizes, and a_c denotes the shortest micro-crack that the local stress can propagate, then the number density of unstable micro-cracks or cleavage initiators, i.e. those that can trigger cleavage, is calculated via

$$\mu_c = \frac{1}{V_0}\int_{a_c}^{\infty} f_c(a)da \tag{1}$$

where V_0 is a scaling volume, typically taken as unit in calculations.

Presently, cleavage fracture is thought to be well approximated by a Poisson's process, as experimental observations at least at low temperatures show agreement with the Poisson postulates: (1) the probability of failure of an elementary volume δV is proportional to the volume; (2) the probability of more than one failure in an elementary volume is of order $o(\delta V)$ and can be assumed zero; and (3) the particle rupture events in non-overlapping volumes are independent. The first postulate gives the elementary probability of failure as $\delta P_f = \mu_c \delta V$. The second postulate yields the condition $\delta P_f \ll 1$. The third postulate is strictly speaking applicable to cleavage at sufficiently low temperatures, and there is experimental evidence that it becomes increasingly violated at higher temperatures or larger scale plasticity.

The existing local approaches, however, rely on the third postulate as it allows for using the weakest-link statistics and the first two postulates to calculate the probability of failure of arbitrary volume, V, by

$$\begin{aligned} P_f(V) &= 1 - \prod (1 - \delta P_f) = 1 - \exp[-\sum \delta P_f] \\ &= 1 - \exp\left[-\int_V \mu_c dV\right], \end{aligned} \tag{2}$$

where the product of elementary survival probabilities in the first expression and the sum of elementary failure probabilities in the second expression is over all elementary volumes in V.

Calculations of component's probability of cleavage fracture by Eq. (2) will be as realistic as is the assessment of the number density of cleavage initiators, μ_c. This depends on the knowledge of how particular mechanical fields determine the critical micro-crack size, a_c, and the probability density of eligible micro-crack sizes, $f_c(a)$.

2.2. Critical micro-crack size

The critical micro-crack size can be calculated from a Griffith-like criterion for unstable growth, e.g. for a penny-shaped crack formed by rupture of a particle the critical size is

$$a_c = \frac{\pi E \gamma}{2(1-\nu^2)\sigma_1^2}, \tag{3}$$

where E and ν are the elastic modulus and Poisson's ratio of the material, respectively, σ_1 is the maximum principal stress, and γ is a measure of fracture energy. Assuming constant fracture energy, equal to the free surface energy of the material, γ_s, provides a good approximation for analysing cases with limited plasticity, such as cleavage at very low temperatures and high crack tip constraint conditions. Plasticity contribution to fracture energy might become important at higher temperatures and lower crack tip constraints.

The first local approach to cleavage fracture proposed by the Beremin group [10], along with developing the statistical argument in the previous sub-section, made one suggestion for taking into account the effect of plastic strains by

$$\gamma = \gamma_s e^{\frac{\varepsilon_1}{2}}, \tag{4}$$

where ε_1 was the maximum principal strain. Another plasticity correction to the fracture energy has been proposed more recently based on equivalence between the real but plastically blunted micro-crack and a larger imaginary elastic micro-crack [11]

$$\gamma = \gamma_s \left[1 + \left(\frac{\pi E \varepsilon_1^p}{4(1-\nu^2)\sigma_1^2}\right)^2\right]^{1/2}, \tag{5}$$

where ε_1^p is the maximum principal plastic strain. The effect of both corrections is in increasing the critical micro-crack size with increasing plastic deformations. A different approach is to define the fracture energy as a function of temperature, rather than indirectly via the plastic strains [12].

The experiments reported in this work and analysed with local approaches were conducted at a sufficiently low temperatures to justify the use of a constant value $\gamma = \gamma_s$. The application of the corrections given by Eqs. (3) and (4) has been found to yield negligible changes to the predictions.

2.3. Probability density of eligible micro-cracks

Assessing the probability density of eligible micro-crack size, $f_c(a)$, for any possible mechanical fields is quite challenging due to limited experimental data. Early experimental works, e.g. [13] and [14], are frequently cited for demonstrating a clear link between the level of plastic strain and the number of micro-cracks formed by rupturing particles, including the effect of temperature and the size distribution of micro-cracks provided in [13]. However, the information obtained in these works is not sufficient to draw conclusions about $f_c(a)$ as a function of the mechanical fields ahead of macroscopic cracks. Firstly, the results reported in these works are obtained by uniaxial tension of flat specimens, i.e. under very specific stress conditions not present in front of a crack. Secondly, the results come from counting all micro-cracks, of which the eligible micro-cracks are a sub-set depending on the local mechanical conditions. This lack of knowledge makes it necessary to test different possibilities for the functional form of $f_c(a)$, as far as these remain consistent with the limited experimental data.

Considering firstly that $f_c(a)$ should be zero in the absence of plastic strains, the Beremin group's original suggestion [10] was that within the plastic zone ahead of a macroscopic crack $f_c(a)$ was approximated by a power law $(a_0/a)^\beta$ representing the tail of the particle size distribution $f_p(a)$. Here a_0 and β are the scale and shape parameters, respectively. This is equivalent to the assumption that all particles in the tail are converted into eligible micro-cracks with the onset of plasticity. If $c(\varepsilon_p)$ is a function representing the effect of plastic strain on the conversion rate of particles into eligible micro-cracks, then for the original Beremin model $c(\varepsilon_p) = H(\varepsilon_p)$, where $H(x)$ is the Heaviside step function.

A recent review of the local approaches to fracture [15] lists a number of proposals for the functional form of $c(\varepsilon_p)$ intended to improve on the original Beremin model in accordance with the experimental evidence such as [13] and [14]. One of these is the power law given by

$$c(\varepsilon_p) = \varepsilon_p^\alpha, \tag{6}$$

where α is a parameter requiring calibration, along with the scale and shape of power law approximating the tail of the particle size distribution. Albeit used occasionally in previous works, Eq. (6) does not appear to be physically and mathematically fit for purpose. Since $c(\varepsilon_p)$ is intended to represent the ratio between eligible micro-cracks and existing particles, it must be within the interval [0, 1], a condition which Eq. (6) cannot fulfil everywhere in the plastic zone ahead of a crack.

Another proposal reviewed in [15] is an exponential law given by

$$c(\varepsilon_p) = 1 - exp(-\lambda\varepsilon_p), \tag{7}$$

where λ is a parameter requiring calibration. Eq. (7) fulfils mathematically the requirement to represent a ration between eligible micro-cracks and existing particles, and it will be used in the present work. It should be noted that the use of Eqs. (6) and (7) as corrections for plasticity has been demonstrated e.g. in [16] and [17].

The eligible micro-cracks according to the Beremin model and its modifications to account for plasticity can now be written in a general form

$$f_c(a) = c(\varepsilon_p)(a_0/a)^\beta. \tag{8}$$

2.4. Density of cleavage initiators and Weibull stress

Assuming a constant fracture energy and using Eqs. (3) and (8) to perform the integration in Eq. (1) leads to an expression for the number density of cleavage initiators as a power law of the maximum principal stress

$$\mu_c = \frac{1}{V_0} c(\varepsilon_p)\left(\frac{\sigma_1}{\sigma_u}\right)^m, \tag{9}$$

where the shape parameter $m = 2\beta - 2$, and the scale parameter σ_u collects the elastic properties, the fracture energy, and the scale of the power law.

In some cases of non-constant fracture energy, e.g. Eq. (4), the functional form of Eq. (9) can be recovered. Specifically for Eq. (4) the plastic strain effect on fracture energy can be assigned to $c(\varepsilon_p)$, which in fact has been done in [10]. It should be noted, however, that the plastic strain effect on fracture energy (concerning propagation of eligible micro-cracks) is principally different from its effect on density of eligible micro-cracks (concerning generation of these), and it is preferable to explicitly state the two contributions.

Contrary to Eq. (4), Eq. (5) does not allow for arriving at the form given by Eq. (9) and in such cases the density of cleavage initiators needs to be calculated by numerical integration of Eq. (1) [11]. One strength of this approach is that it allows for treating arbitrary probability density functions of eligible micro-cracks, e.g. linked to experimentally measured particle sized distributions, followed by direct calculation of probability of failure by Eq. (3) as applied in [11] and [12]. The price paid for this flexibility is that the probability of failure does not have the Weibull form achieved by using Eq. (9) as shown below.

Substitution of Eq. (9) into Eq. (1) yields the following expression for the component probability of failure

$$P_f(V) = 1 - \exp\left[-\frac{1}{V_0}\int_V c(\varepsilon_p)\left(\frac{\sigma_1}{\sigma_u}\right)^m dV\right], \tag{10}$$

which can be written as a Weibull distribution, Eq. (11), of an integral stress parameter, σ_w in Eq. (12), known as Weibull stress since [10].

$$P_f(\sigma_w) = 1 - \exp\left[-\left(\frac{\sigma_w}{\sigma_u}\right)^m\right]. \tag{11}$$

$$\sigma_w = \left[\frac{1}{V_0}\int_V c(\varepsilon_p)\sigma_1^m dV\right]^{1/m} \tag{12}$$

The use Eqs. (11) and (12) requires calibration of the shape parameter m, the scale parameter σ_u, and λ in the plasticity correction given by Eq. (7). These are used in the analyses presented in the work and the calibration procedure is explained in Section 5.

3. Experimental programme and results

3.1. Material and specimens

The material used in the experimental programme was a reactor pressure vessel steel A533b Class 1, with chemical composition determined by Energy Dispersive Analysis X-ray (EDAX) and average values from three measurements given in Table 1. Specimens for tensile and fracture toughness tests were machined from a plate of A533b, which, prior to delivery, had been annealed (heated to ~900 °C) for 4.25 h, quenched, tempered at ~650 °C for 6.7 h, air-cooled and cross-rolled. This condition will be referred to as the as-received material. Microscopy of the as-received material revealed areas of ferrite and tempered martensite. Martensite microstructure formed during annealing and quenching as body-centred-tetragonal, changed during tempering by precipitation of carbides into α-ferrite. The important role of carbides in cleavage fracture is well established by numerous previous studies and a vast literature on this subject. These carbide particles appear to be the principal brittle inclusions in the steel, which agrees with the majority of experimental observations and current understanding of mechanisms of cleavage fracture in RPV steels [6–8,13,14]. Readers are referred to the review article of Hahn [18] for a full account of the cleavage fracture mechanism in ferritic steels, including the fundamental role played by carbides at grain boundaries as the key cleavage triggering particles.

The fracture toughness specimens used in the experimental programme were SEN(B) with standard dimensions as per BS7448 [19]: thickness $B = 25$ mm; width $W = 2B = 50$ mm, and span $S = 4W = 200$ mm. With crack depth denoted by a, three types of specimens were used: $a/W = 0.4 (a = 20$ mm), referred to as the high-constraint (HC) specimens; $a/W = 0.2 (a = 10$ mm), referred to as the intermediate-constraint (IC) specimens; and $a/W = 0.05 (a = 2.5$ mm), referred to as the low-constraint (LC) specimens. BS7448 prescribes that a fatigue pre-crack of at least $2.5\%W = 1.25$ mm is grown from a notch and included in the a/W ratio. In order to make a consistently deep

Table 1
Chemical composition (%wt) of A533b Class 1 steel.

C	Mn	Ni	Mo	Si	Cr	Cu	Al	S
0.21	1.57	0.61	0.51	0.41	0.12	0.09	0.05	0.01

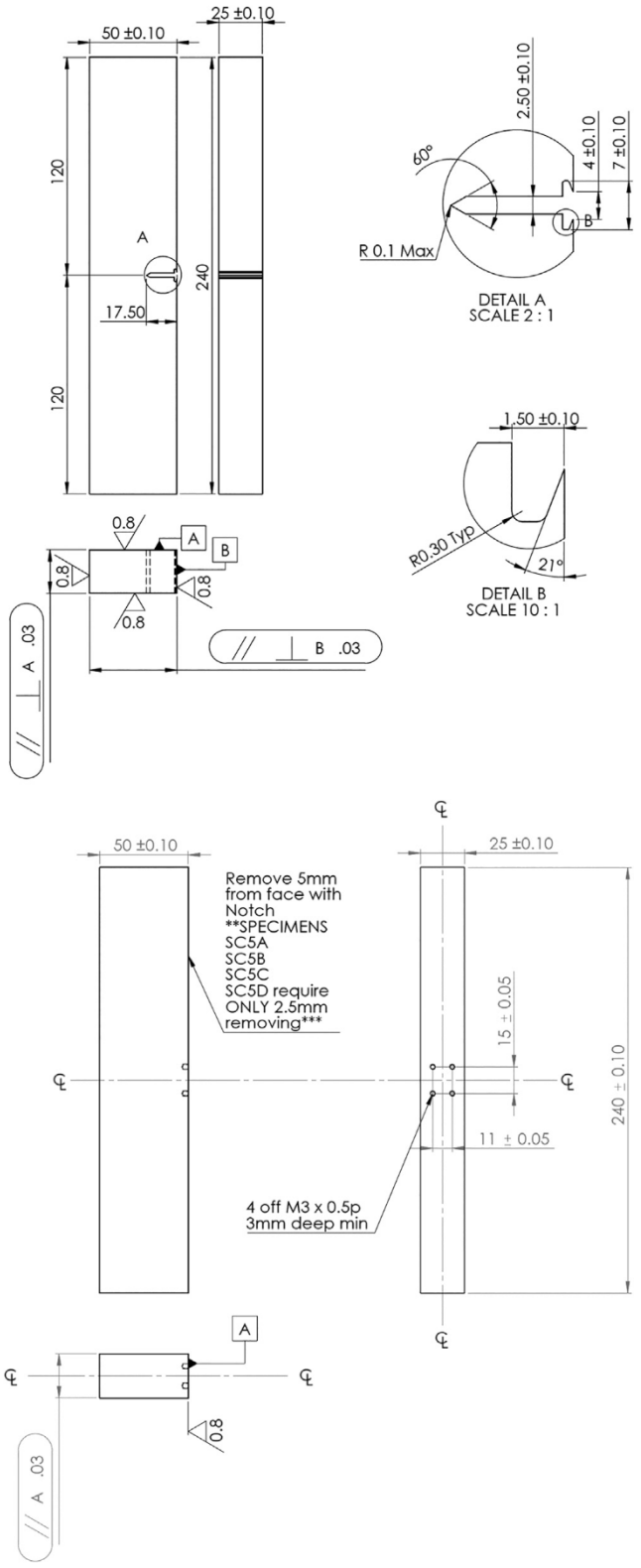

Fig. 1. SEN(B) design with a/W = 0.4 and a/W = 0.05; all dimensions in mm.

fatigue pre-crack across the a/W ratios, and considering that the low-constraint specimen would not allow for the presence of a notch, the fatigue pre-crack depth was selected to be $5\%W = 2.5$ mm. For the high- and intermediate-constraint specimens the pre-crack were introduced from notches of 17.5 mm and 7.5 mm, respectively. Details of high-constraint specimen are shown in Fig. 1 (left). For the low-constraint specimens, plates with initial width $W = 55$ mm were used to machine 5 mm notch. After introducing the 2.5 mm pre-crack, the plate face was machined to reduce the width to $W = 50$ mm, thus producing $a/W = 0.05$. Details of low-constraint specimen are shown in Fig. 1 (right).

In addition to fracture toughness tests, tensile tests were carried out according to BS 10002 [20]. The specimens were of standard circular section design, with a gauge diameter of 15 mm and a machined gauge length of 43 mm.

The plate used for specimens machining was with dimensions 1114 × 804 × 70 mm. It was sectioned by a water jet cutter into flat dog-bone specimens and insets, as shown in Fig. 2. The dog-bone specimens were subjected to tensile load at ambient temperature in order to introduce 5% plastic strain approximately uniformly across the gauge. The loading machine was 8806 2.5MN Instron™, and the strain was controlled by four strain gauges, spaced equidistantly along the specimens. The loading was applied at a displacement rate of 0.5 mm/min, interrupted when the average reading of the four gauges was 55000 $\mu\varepsilon$ (5.5%, assuming elastic strain of 0.5%), and release following interruption.

The insets and the plastically deformed dog-bone specimens were used to machine SEN(B) specimens with the three crack depths as described above. A total of 60 fracture toughness specimens were prepared for this study – 10 specimens of each crack depth from as-received and pre-strained materials. Three tensile specimens of as-received and six from pre-strained were prepared from broken SEN(B) $a/W = 0.4$ far from the crack plane, to ensure as little effect of crack tip plasticity as possible on the measured stress-strain curves.

3.2. Fracture toughness tests and results

Fatigue pre-cracking was carried out on Ansler ± 100 kN vibraphore machines at room temperature. Each pre-crack was completed in 4 steps (0.625 mm each). The specimens had lines drawn on at each step, and the load was stepped down incrementally from a far $K_I = 25\text{Ã}\cdot 20$ MPa$\sqrt{\text{m}}$, such that no residual stress would be introduced, and there would also be minimal plasticity introduced at the crack tip. The crack growth was observed on video cameras and after the final step had been completed a final measurement of the crack length was taken, on both sides. Table 2 shows fatigue pre-cracking data from this process – mean and standard deviation of number of cycles and crack depths. All initial crack depths for the tested specimens are listed in tables of Appendix A. The standard deviation in the number of cycles for the required crack depth is due to variations in the applied stress intensity amplitude between different specimens of the same type, as well as variations in their local microstructures.

Fracture toughness testing was carried out on a Schenk 250 kN testing machine. To ensure that the failure mode of the low-constraint specimens was cleavage, all tests were performed at −140 °C. The specimens were cooled using liquid nitrogen in an environmental chamber, with the temperature monitored by a thermocouple, which was installed in contact with the specimen. To ensure that the entire specimen had cooled to the appropriate temperature, the cooling continued after the temperature reached −140 °C for 1 min/mm thickness of the specimen. Once the specimen was sufficiently cooled the test was carried out. Load was applied as shown in Fig. 3, until the specimen failed. The load and crack mouth opening displacement (CMOD) were recorded. Typical load-CMOD traces for the three constraint and two material conditions are shown in Fig. 4.

In all cases, except for one LC specimen of as-received material, the test pieces broke cleanly in two. Following cleavage, measurements of the crack were taken at 9 equidistant points through the thickness of the specimen, starting from a position of 0.01B into the thickness of the specimen, as required by ASTM 1921 [21]. This analysis was used to assess the extent of ductile tearing during the testing if applicable, and the fatigue pre-crack dimensions. All cases met the conditions for

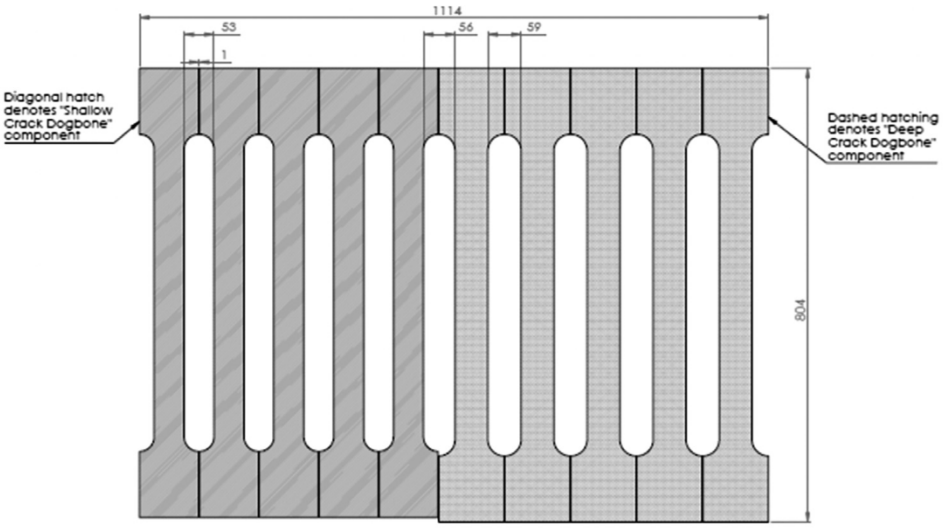

Fig. 2. Cut design to produce dog-bone specimens for pre-straining. Insets (white areas) used for SEN(B) specimens of as-received material. Shallow crack refers to dog-bones used for SEN(B) specimens with $a/W = 0.05$; Deep crack refers to dog-bones used for SEN(B) specimens with $a/W = 0.2$ and $a/W = 0.4$.

Table 2
Fatigue pre-crack data.

Specimen type	Mean (SD) number of cycles to 2.5 mm crack	Mean (SD) measured crack depth, mm
$a/W = 0.4$ as-received	327,329 (120,837)	19.85 (0.19)
$a/W = 0.2$ as-received	298,958 (55,204)	9.93 (0.08)
$a/W = 0.05$ as-received	198,989 (103,728)	2.54 (0.05)
$a/W = 0.4$ pre-strained	222,130 (38,300)	20.06 (0.06)
$a/W = 0.2$ pre-strained	196,220 (11,855)	10.06 (0.07)
$a/W = 0.05$ pre-strained	129,195 (38,300)	2.50 (0.04)

cleavage fracture. Further details for all specimens, including measured initial crack lengths, loads and crack mouth opening displacements at failure, as well as calculated fracture toughness values and deformation limits, are provided in Appendix A. The fracture toughness values and the specimen measuring capacity (as characterized by the deformation limit, $M = b{\cdot}\sigma_y/J$, where b is the remaining crack ligament) were calculated as per ASTM 1921 [21]. The calculated deformation limits are well above the standard requirement of 30–60 proving that all

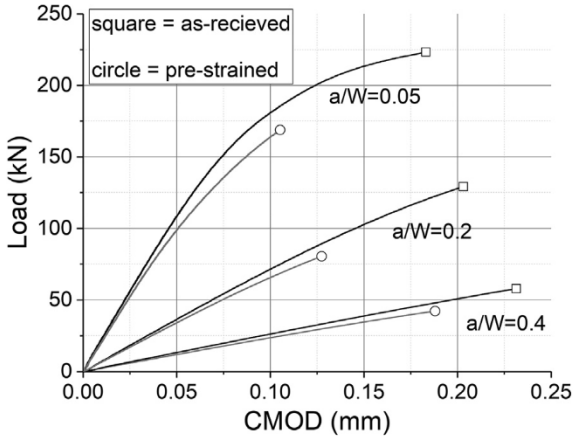

Fig. 4. Typical Load-CMOD records from specimens with the three constraint and the two material conditions.

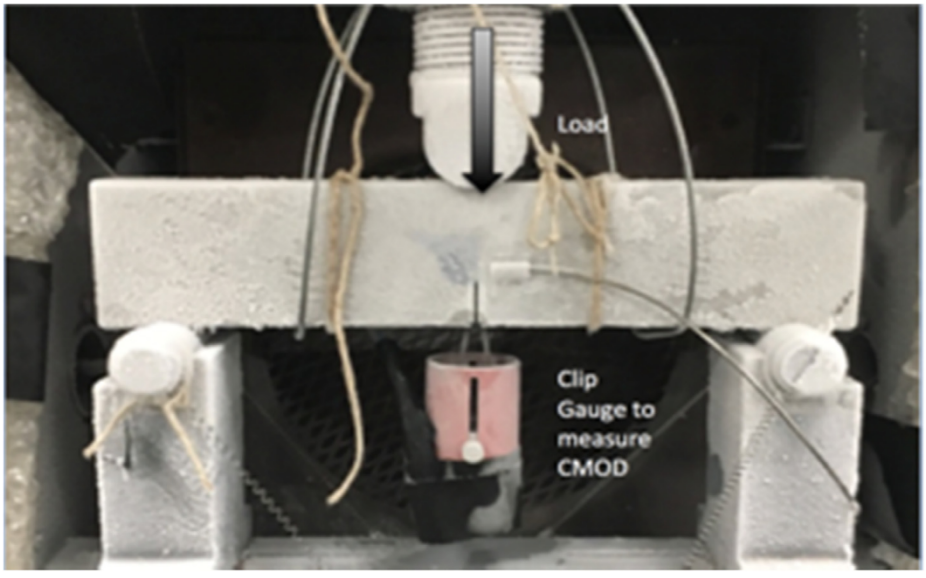

Fig. 3. SEN(B) specimen in testing machine.

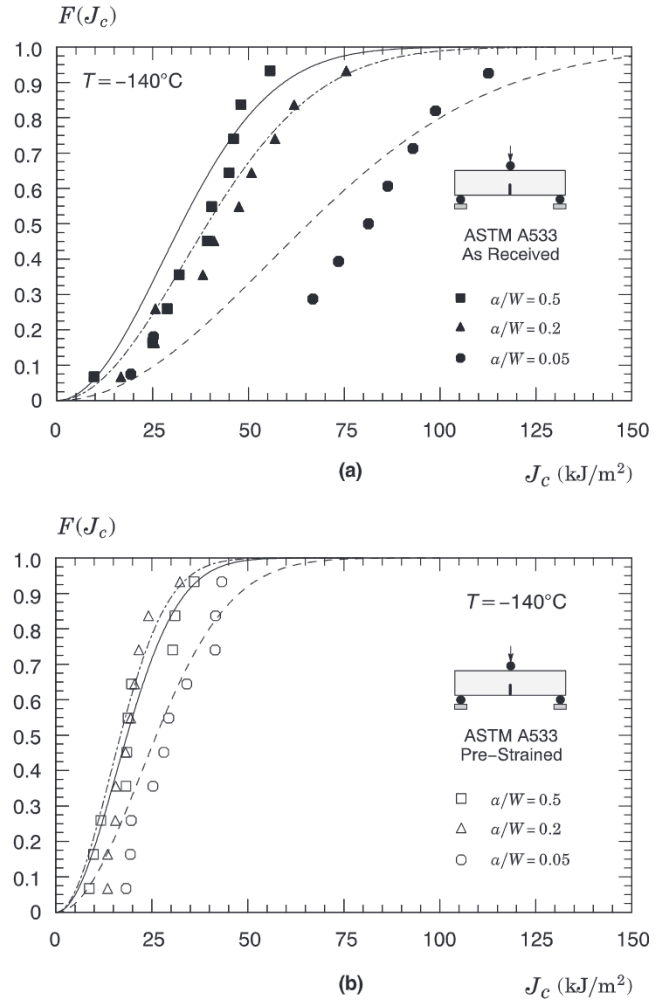

Fig. 5. Cumulative Weibull distribution of experimentally measured J_c-values of the tested A533 steel: (a) As-received material. (b) Pre-strain condition.

specimens clearly exhibited cleavage fracture under stress-controlled, small-scale yielding conditions.

The cumulative Weibull distribution of the measured J_c-values for the tested geometries in both material conditions is displayed in Fig. 5. These toughness distributions are employed in the fracture predictions presented in Section 5. The solid symbols in the plots represent the experimentally measured fracture toughness J_c-values for each test specimen. The cumulative probability, $F(J_c)$, is derived by ranking the J_c-values in ascending order and using the median rank position defined in terms of $F(J_{c,k}) = (k - 0.3)/(N + 0.4)$, where k denotes the rank number and N defines the total number of experimental toughness values [22].

The fitting curves to the experimental data shown in Fig. 5 describe a two-parameter Weibull distribution [22] for J_c-values given by

$$F(J_c) = 1 - \exp\left[-\left(\frac{J_c}{J_0}\right)^{\alpha}\right], \tag{13}$$

where α is the Weibull modulus (which describes the scatter in test data) and J_0 is the scale parameter, often interpreted as a characteristic toughness, defining the J_c-value for which $F(J_c \le J_0) = 63.2\%$. A parameter estimation of the data set shown in Fig. 5 is performed by adopting the maximum likelihood (ML) method [22] with a fixed value of $\alpha = 2$ as the Weibull modulus for the Weibull distribution describing the data set of J_c-values under small scale yielding conditions [9,23].

Table 3 provides the ML estimates of the Weibull parameters (α, J_0), including the 90% confidence intervals for J_0, for the measured distributions of J_c-values for each specimen geometry. The table also includes a column of predicted fracture toughness values, which will be discussed in Section 5. The significant features include: (1) the characteristic toughness of the Weibull distribution for the test data of the as-received condition shows a relatively strong dependence on specimen geometry; (2) pre-strain decreases fracture toughness for a given a/W ratio with respect to the corresponding geometry for the as-received material; and (3) the characteristic toughness of the Weibull distribution for the test data of the pre-strain condition is weakly sensitive to specimen constraint. This last feature can be seen in Fig. 5(b) in which the toughness distributions for all pre-strain geometries are relatively close to each other, clearly evidencing that pre-strain offsets the potential effects of constraint on fracture toughness. To facilitate comparison between different cases, the data from the Appendix and Table 3 is plotted in Fig. 6.

3.3. Tensile tests and results

Tensile tests were carried out on a Zwick tensile testing machine with a 50kN load cell at two temperatures −140 °C and 20 °C. Tests at −140 °C were used to obtain deformation data for finite element analysis of tested fracture toughness specimens. Tests at 20 °C were used to corroborate the effect of pre-straining on the deformation properties observed at −140 °C and discussed below. All tests were displacement controlled at a strain rate of 0.025%/sec using TestXpertII software inbuilt to the test system. Prior to all testing pertinent measurements were carried out including gauge diameter measured to a resolution of 10 μm. The strain was measured through an extensometer up to 1.5%, and then through crosshead travel.

The full true stress-true strain curves for all tested specimens at −140 °C are shown in Fig. 7(a). Essential data obtained standardly from these tests is shown in Table 4: Young's modulus, E, yield (proof) stress at 0.2% plastic strain, $\sigma_y = \sigma_{0.2}$, and ultimate tensile strength, σ_{UTS}. Initially, based on the full-stress-strain curves the Young's modulus was assumed unchanged with pre-straining, and measured yield stress and ultimate tensile strengths were used to formulate directly Ramberg-Osgood material models for the as-received and pre-strained conditions. However, their use in simulating the response of SEN(B) specimens produced load-CMOD traces in clear disagreement with the experimental traces shown in Fig. 4. Specifically, the simulated responses were substantially stiffer than the experimental ones. This prompted examination of the materials' behaviour at small strains shown in Fig. 7(b). The recorded responses show approximately linear behaviour for both material conditions up to a proportionality stress, σ_0, lower than the standardly defined yield stress $\sigma_y = \sigma_{0.2}$. Notably, while the yield stress for the pre-strain material is indeed higher than the corresponding value for the as-received, Fig. 7(a), a closer look at the stress-strain response within a strain range of ~0.2–0.5%, Fig. 7(b), does reveal a marked difference in the proportionality limit behaviour, and thus on the elastic region, between the two states. This, in turn, likely affects the load-CMOD responses for the SE(B) specimens.

Considering that accurate load-CMOD responses, and consequently crack tip stress fields, are essential prerequisite for implementing a local approach to fracture, the Ramberg-Osgood model was replaced with an elastic-plastic hardening model, where the behaviour is elastic up to a proportionality stress σ_0, and the hardening behaviour is provided in a tabular form as stress versus plastic strain taken from the experimental curve post proportionality limit. Lüder's strain region, observed in Fig. 7, while typical for this approximately uniform stress condition, is not observed in the presence of stress gradients, i.e. the conditions ahead of microscopic crack. Hence, for the purposes of finite element analysis of SEN(B) specimens, the region was removed from the formulation of the stress-plastic stain relation by shifting the plastic strains in the hardening branch by the length of the Lüder's strain region. Details of the tabulated stress-plastic strain are not given here. It is acknowledged that accurate determination of a proportionality limit is

Table 3
Maximum likelihood estimates of parameter J_0 for the measured distributions of J_c-values of the tested A533 steel for each specimen geometry and condition.

Specimen type	α	J_0, kJ/m^2	90% confidence bounds for J_0, kJ/m^2	Predicted J_0, kJ/m^2
$a/W = 0.4$ as-received	2	39.1	(28.3, 54.5)	39.1 (used)
$a/W = 0.2$ as-received	2	47.2	(34.2, 65.9)	45.7
$a/W = 0.05$ as-received	2	78.9	(55.8, 112.9)	78.9 (used)
$a/W = 0.4$ pre-strained	2	22.3	(16.7, 31.1)	22.8
$a/W = 0.2$ pre-strained	2	20.2	(14.7, 28.2)	26.1
$a/W = 0.05$ pre-strained	2	31.5	(22.8, 43.9)	32.6

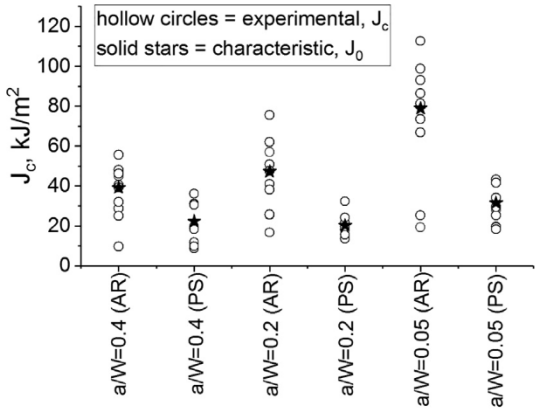

Fig. 6. Distribution of measured fracture toughness values J_c (hollow circles), and the ML estimated J_0-values (black squares) for the three constraint and two material conditions.

not an established process. Approximate values are determined from the strain-strain curves as the values where the recorded trace deviates more than 1% from the elastic line, see Fig. 7(b). These values are recorded in Table 4. The use of the described model provided excellent agreements between the simulated and measured load-CMOD traces.

The tensile test results at −140 °C suggested that the pre-straining of the material caused stiffness reduction as well as reduction of the proportionality stress. For this reason, tests at room temperature were performed with results reported also in Table 4. These confirm the observation at the cryogenic temperature of reduced stiffness and proportionality stress σ_0 due to pre-straining. Similar observations have been reported previously. For example, Benito et al. [24] observed through standard tensile testing of pure iron a reduction in the Young's modulus from 210 to 196 GPa at 6% plastic strain. Yang et al. [25] reported a more significant reduction in modulus in SPCE carbon steel sheet metal, through both macroscopic tensile testing and nano-indentation of the material with a spherical indenter. Both papers offered an explanation for a reduction in elastic modulus caused by an increase in dislocations and dislocation movement due to pre-straining. In a recent paper Chen et al. [26] demonstrated further this reduction by comparing results of various methods of modulus measurement, including measurement of resonant frequencies and ultrasonic pulses in the material, alongside mechanical tensile testing. In addition to the explanations offered in [24–26], we suggest a further possibility. The pre-straining to 5% plastic strain was sufficient to rupture second-phase particles in the material, those of sizes in the tail of the particle size distribution. For example, according to Gurland's results [14], which have been obtained under conditions similar to the pre-straining used here, 5% strain converts 1% of all particles into micro-cracks. The presence of such micro-cracks, from one side represents damage, i.e. lower elastic modulus, and from another new sources of dislocations, i.e. lower proportionality limit.

Irrespective of the probable reason for stiffness and proportionality limit reduction, we emphasize that the experimental stress-strain data is just a means to obtain accurate resolutions of the near-tip stress and strain field ahead of crack tip. Consequently, it is far more important to have a good agreement between the numerical and the measured load-CMOD curves than strictly relying on the measured flow properties for the material. The approach can be considered as a "phenomenologically-calibrated stress-strain response" for use in FEA of cracked components.

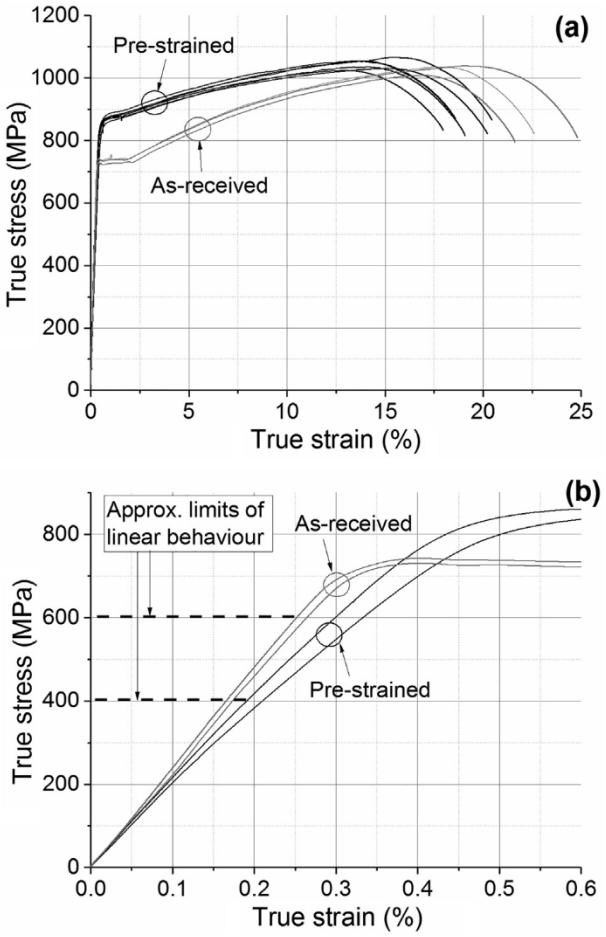

Fig. 7. Experimental stress-strain response of as-received and pre-strained A533b material at −140 °C: (a) full curves; (b) small-strain responses.

4. Finite element modelling

Nonlinear finite element analyses were performed with 3D models of SEN(B) specimens having the same dimensions as the tested specimens: $W = 25$ mm, $B = W/2$, $S = 4W$ (no side grooves). Abaqus/CAE environment [27] was used to build up and mesh the models and set up the mechanical properties and boundary conditions.

Symmetries with respect to crack plane and mid-thickness were used to construct one-quarter models of the SEN(B) specimens for computational efficiency. The models were meshed using 3D 8-node

Table 4
Tensile data from as-received and pre-strained A533b at two temperatures. Data from tests at −140 °C is used in FEA material behaviour formulation; Flow stress at −140 °C is used in the scaling method in Section 5; Data from tests at 20 °C is used to illustrate a reduction of Young's modulus and proportionality stress similar to the tests at −140 °C.

	As-received material	Pre-strained material
Tests at −140 °C, data used in FEA		
Young's modulus, E, GPa	215.3	203.3
Poisson's ratio, ν	0.3	0.3
Proportionality stress, σ_0, MPa	600	400
Proof stress (at 0.2% ε_p), σ_y, *MPa*	734.0	841.8
Ultimate tensile strength, σ_{UTS}, *MPa*	875.0	905.5
Flow stress, $\sigma_f = (\sigma_0 + \sigma_{UTS})/2$, *MPa*	735	660
Tests at 20 °C, data used for comparison		
Young's modulus, E, GPa	207.7	197.5
Proportionality stress, σ_0, MPa	450	250
Proof stress (at 0.2% ε_p), σ_y, *MPa*	511.7	680.1
Ultimate tensile strength, σ_{UTS}, *MPa*	651.8	693.8

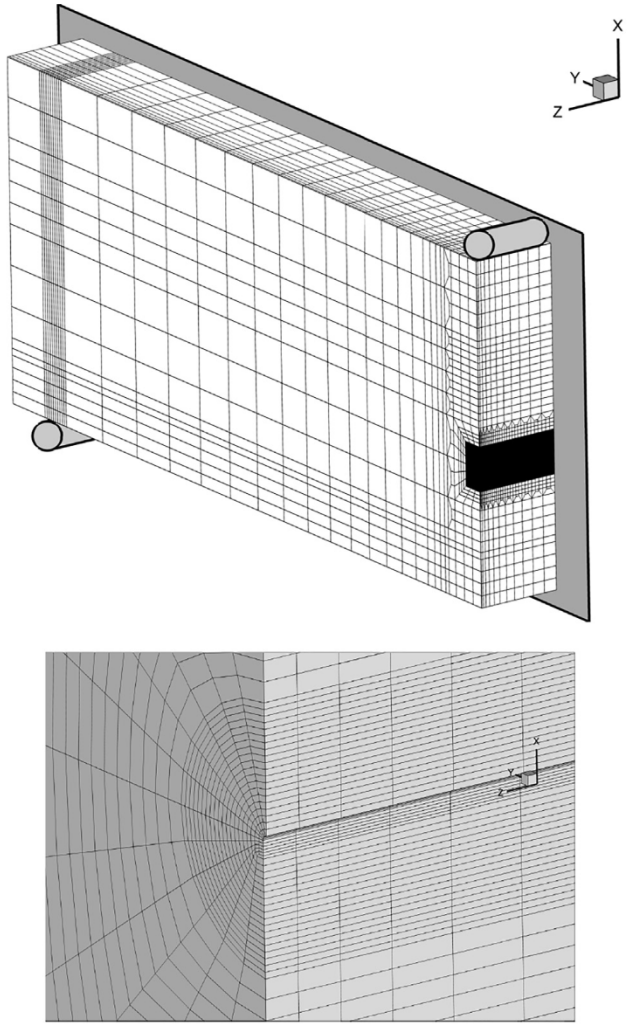

Fig. 8. Quarter-symmetric finite element model of the deeply-cracked SEN(B) specimen with detail of the crack tip mesh.

linear brick elements (C3D8). The crack tip was represented as a notch with radius $\rho = 10$ μm to allow for performing finite strain analysis. A focused ring of elements surrounding the crack tip was used to define contours for J-integral calculations. An illustration of the one-quarter model and the near tip mesh for the deeply-cracked SEN(B), $a/W = 0.4$, is given in Fig. 8. The finite elements models for the other crack sizes, $a/W = 0.05$ and $a/W = 0.2$ have similar features.

The meshes had 30 variable thickness layers defined over the half-thickness $(B/2)$; the thickest layer was defined at $Z = 0$ with thinner layers defined near the free surface $(Z = B/2)$ to accommodate strong Z variations in the stress distribution. The quarter-symmetric, 3D model for this specimen had approximately 53,800 nodes and 47,500 3D elements.

The material elastic and flow properties match those for the A533b steel tested at $T = -140$ °C as depicted in Fig. 7. The flow behaviour was provided to Abaqus in a tabular form, i.e. a piece-wise linear relation between stress and plastic strain. This piecewise-linear representation of the measured true stress- true plastic strain curve offered a better description of the experimental data as well as an improved computational efficiency compared to traditionally used power law representations, such as Ramberg-Osgood. The elastic-plastic constitutive model employed here follows a flow theory with conventional Mises plasticity with finite strain settings (NLGEOM in Abaqus).

The finite element models were loaded by displacement increments imposed on a frictionless rigid cylinder using general contact available in Abaqus. Implicit integration scheme (Abaqus/Standard) was used to perform all analyses. Abaqus/Standard employs a domain integral method or virtual crack extension approach [28] for numerical evaluation of the J-integral to provide pointwise values of J across the crack front at each loading level. The numerical J values used correspond to the thickness-average J for each cracked specimen.

5. Results and discussion

5.1. Calibration of the modified Weibull stress parameters

Calibration of the parameters m and λ defining the Weibull stress given by Eqs. (12) and (7) is a key step in the procedure to predict the effects of constraint and pre-strain on fracture toughness. The Weibull shape parameter, m, plays a major role in the process to correlate toughness values across different crack configurations as this parameter alters the $\sigma_w - J$ trajectories needed to correlate the Weibull stress at fracture. The λ parameter controls the function $c(\varepsilon_p)$, which accounts for the effect of plastic strain on conversion of particles into eligible micro-cracks. Because m and $c(\varepsilon_p)$ characterise the shape of the size distribution and the density of the cleavage initiators, respectively, their evaluation can be made by a two-step process derived from fracture toughness data at different constraint conditions in combination with detailed finite element analyses. Here, these parameters are determined using a procedure similar to the calibration scheme based on a toughness scaling methodology (TSM) employed in [16].

Firstly, the parameter m is determined to establish the best correction for cleavage fracture toughness data measured from two sets of test specimens exhibiting largely contrasting toughness behaviour, using $c(\varepsilon_p) = H(\varepsilon_p)$ in Eq. (12). By interpreting σ_w as an *effective* crack driving force, the calibration procedure is based on the assumption that cleavage fracture occurs at one and the same critical value of the effective crack driving force σ_w^c across different crack configurations. This condition must be met, even though the loading parameter, measured here by the J-integral, may vary widely due to constraint loss. In the present application, calibration of parameter m is conducted for the as-received condition by scaling the characteristic toughness, J_0, of the measured toughness distribution for the very shallow crack, $a/W = 0.05$ (denoted here by J_0^B), to its equivalent value of toughness distribution for the deep crack, $a/W = 0.4$ (denoted here as J_0^A). The calibration process consists of minimizing the residual $R(m) = (J_{0,m}^B - J_0^B)/J_0^B$, where $J_{0,m}^B$ is readily interpreted as the corrected characteristic toughness, J_0^B, derived from the $\sigma_w - J$ relation for the calibrated value of the Weibull modulus, m. Following this procedure to correct $J_0^{a/W=0.05}$ to its equivalent characteristic toughness $J_0^{a/W=0.4}$ yields a calibrated value of

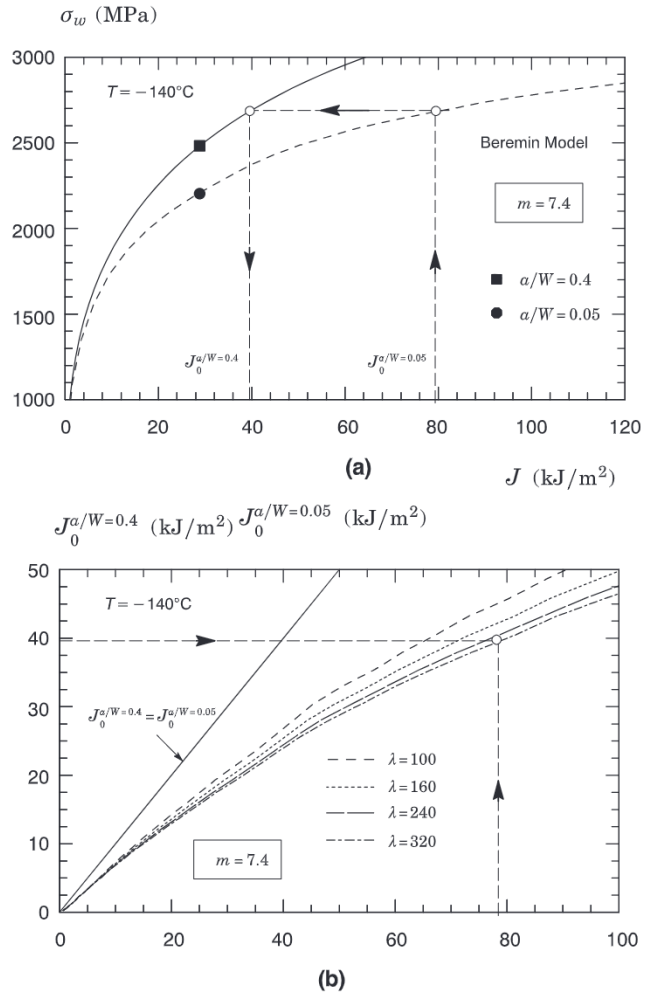

Fig. 9. Calculated $\sigma_w - J$ trajectories for the SEN(B) specimens with $a/W = 0.4$ and $a/W = 0.05$ $T = -140$ °C with $c(\varepsilon_p) = 1$ and $m = 7.4$ (a); and constraint correlations $J_0^{a/W=0.05} \rightarrow J_0^{a/W=0.4}$ for varying values of parameter λ (b).

$m = 7.4$.

The final result is given in Fig. 9(a), where the evolution of σ_w with increased values of J is shown for $c(\varepsilon_p) = H(\varepsilon_p)$ and $m = 7.4$ in Eq. (12) for both specimen geometries at the test temperature $T = -140$ °C. The arrows in this plot indicate the correlation scheme for parameter J_0 based on a fixed value of σ_w^c at fracture for varying specimen constraint. Further details of m-calibration can be found in the early works [29,30].

With the Weibull modulus thus determined and now assumed fixed throughout the analysis, the calibration process then proceeds by evaluation of the function $c(\varepsilon_p)$ that again provides the best correction for cleavage fracture toughness data measured from the two sets of test specimens utilized at the onset of the calibration procedure using the TSM. Here, the $\sigma_w - J$ relations for a fixed m enable determination of the function $c(\varepsilon_p)$ that provides the best correction $J_0^B \rightarrow J_0^A$ such that the residual, $R[c(\varepsilon_p)] = R(\lambda)$, is minimized. To illustrate the calibration process, Fig. 9(b) provides the constraint correlations $J_0^{a/W=0.05} \rightarrow J_0^{a/W=0.4}$ for varying values of parameter λ. Each curve consists of pairs of J-values for the very shallow and the deep crack SEN (B) specimen, which produce the same Weibull stress, σ_w for a fixed λ-value. Further, within the present context of probabilistic fracture mechanics, each pair $(J_0^{a/W=0.05}, J_0^{a/W=0.4})$ on a given curve defines equal failure probabilities for cleavage fracture. A reference line is shown which defines a unit toughness ratio, i.e. $J_0^{a/W=0.05} = J_0^{a/W=0.4}$. With this process, correction of the characteristic toughness for the shallow crack SEN(B) geometry, $J_0^{a/W=0.05}$, to its equivalent characteristic toughness

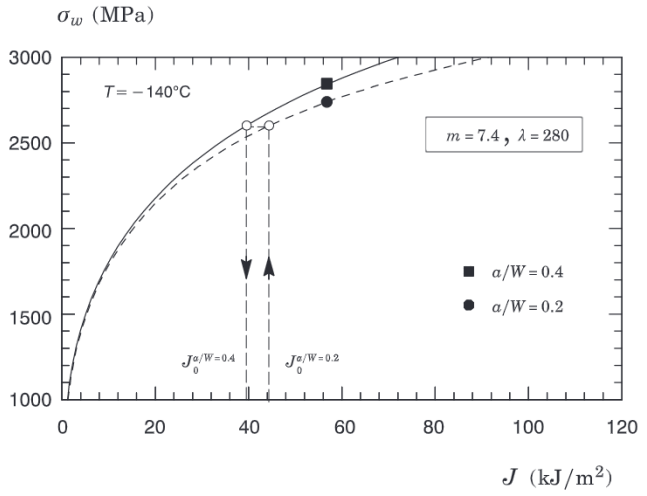

Fig. 10. Prediction of $J_0^{a/W=0.2}$ using $\sigma_w - J$ trajectories for the SEN(B) specimens with $a/W = 0.4$ and $a/W = 0.2$, $T = -140$°C with $\lambda = 280$ and $m = 7.4$.

for the deeply-cracked SEN(B) specimen, $J_0^{a/W=0.4}$, yields $\lambda \approx 280$.

The calibrated m and $c(\varepsilon_p)$ were used to calculate the fracture toughness of the intermediate constraint geometry with as-received material – the procedure is illustrated in Fig. 10 – predicting a fracture toughness value of $J_0^{a/W=0.2} = 45.7$ kJ/m^2. This value is recorded in Table 3 and it can be seen to be very close to the experimental one, albeit slightly underestimating it. It is worth mentioning that using the above calibration procedure with data from the specimens with $a/W = 0.2$ and $a/W = 0.4$, for example, gives a prediction for the fracture toughness of specimens with $a/W = 0.05$ that substantially overestimates the experimental one. Although this process is not demonstrated here, the outcome suggests that the calibration process should be applied for as large difference in constraint as experimentally possible, in which case the toughness values for intermediate constraint conditions would be predicted sufficiently accurately. Further, the calibration between two constraint conditions is not likely to provide acceptable predictions for constraints outside the region used for calibration.

The adopted procedure is relatively simple and, perhaps most importantly, does preserve the character of the parameter m in describing the shape of the size distribution of cleavage initiators. It is worth mentioning, however, that the calibrated parameters, m and $c(\varepsilon_p)$, are not fully matching the physical meanings assigned to them in Section 2. Because of the nature of the calibration process adopted here, which relies on the TSM and macroscopic measures of fracture toughness, m and $c(\varepsilon_p)$ should be interpreted as *phenomenological* parameters that bring fracture toughness predictions into agreement with experimental fracture data, rather than accurate descriptors of the metallurgical features and micro-mechanical processes.

5.2. Predictions of constraint and pre-strain effects on fracture toughness

Verification analyses of the σ_w-methodology described here addresses predictions of pre-strain effects on the fracture toughness distributions for the tested A533 pressure vessel steel. As discussed above, the interpretation of parameter σ_w as an *effective* crack driving force in connection with the notion of a critical value of the Weibull stress at cleavage fracture, σ_w^c, enables multiscale correlations between the measured toughness distribution across different specimen configurations and material conditions. Here, the measured distribution of cleavage fracture toughness values for the specimens of pre-strained material is predicted based on the measured fracture toughness distribution for the deeply-cracked SEN(B) specimen in the as-received condition.

The correlative procedure to obtain the toughness corrections

follows similar protocol for the TSM outlined previously but with additional considerations to define the effective crack driving force applicable to both material conditions. Because of differences in flow properties between the as-received and pre-strained materials, it will no longer be the case that a fixed, absolute value of σ_w^c holds for each condition. Indeed, the clear trend of decreased fracture toughness with pre-strain observed in Fig. 5(b) appears consistent with a decreased crack driving force triggering cleavage fracture. This is further supported by the discussion offered in Section 3.3, where the reduction of the elastic modulus and the proportionality stress due to pre-straining is attributed to early dislocation mobility and possibly a generation of ruptured particles. This process clearly changes the "initial conditions" for the calculation of an *effective* crack driving force.

In order to capture the difference between the initial conditions of the as-received and the pre-strained material, a simple scaling process is proposed here, based on the material flow stress $\sigma_f = (\sigma_0 + \sigma_{UTS})/2$, where σ_0 and σ_{UTS} denote the proportionality stress and the ultimate tensile strength, respectively, as given in Table 4. The proposal is that the cleavage fracture for the two material conditions occurs at one and the same non-dimensional critical Weibull stress, defined by

$$\bar{\sigma}_w^c = \sigma_w^c/\sigma_f. \tag{14}$$

A fundamental assumption of the Weibull stress methodology lies in the interpretation of σ_w as the crack driving force, which reaches a critical value σ_w^c at cleavage fracture. For the same material at a fixed temperature, the scaling model requires the attainment of the critical value to trigger cleavage fracture across different specimen configurations even though the loading parameter (measured by J in the present work) may vary widely due to constraint loss. In the present context, it becomes clear that the crack driving force, phrased in terms of σ_w, must scale with the material's flow properties, more specifically σ_0, such that the critical value, σ_w^c, at cleavage fracture is attained in fracture specimens with different pre-strain conditions. Indeed, such arguments can be brought to bear on the adopted approach by simply examining the stress integral associated with σ_w given by Eq. (12). Since σ_w is defined by the principal stress raised to a power (the Weibull modulus, m) integrated over the near-tip fracture process zone and, further, since the principal stress, σ_1, scales with the material's flow properties, it becomes clear that pre-strain will influence the near-tip stress distribution which, in turn, will affect the σ_w-value at a fixed J for a given specimen geometry. Thus, the toughness scaling methodology in connection with effects of pre-strain on fracture toughness can be readily phrased in terms of a non-dimensional Weibull stress thereby including the potential influence of varying flow properties arising from pre-strain on the crack driving force, characterized by the Weibull stress in the present context. Clearly, the non-dimensional Weibull stress has no direct physical meaning, and it is used only for the purposes of predicting the change of toughness due to pre-straining. It could be considered, however, as a modifier to the Weibull shape parameter σ_u in Eq. (11), arising from the changes in deformation properties due to pre-straining. Fig. 11 shows the evolution of the non-dimensional Weibull stress, $\bar{\sigma}_w = \sigma_w/\sigma_f$, with J for the cases under consideration using the calibrated model parameters, $m = 7.4$ and $\lambda = 280$. It should be noted that the pre-strain is not included in the calculation of this Weibull stress, i.e. the plastic strain used in Eq. (7) for plasticity correction is the one obtained with FEA with the deformation properties of the pre-strained material given in Table 4. An attempt to include the pre-strain as an addition to the calculated plastic strain led to incorrect predictions. Using $J_0 = 39.1$ kJ/m^2 as the base value corresponding to the deeply-cracked SEN(B) specimen in the as-received condition, a simple procedure defines the corresponding J_0-values for the pre-strain geometries as indicated in the plot. The characteristic fracture toughness values predicted by this procedure are included in Table 3.

Fig. 12 shows the predicted Weibull cumulative distribution of J_c-values for specimens of pre-strained material based on the

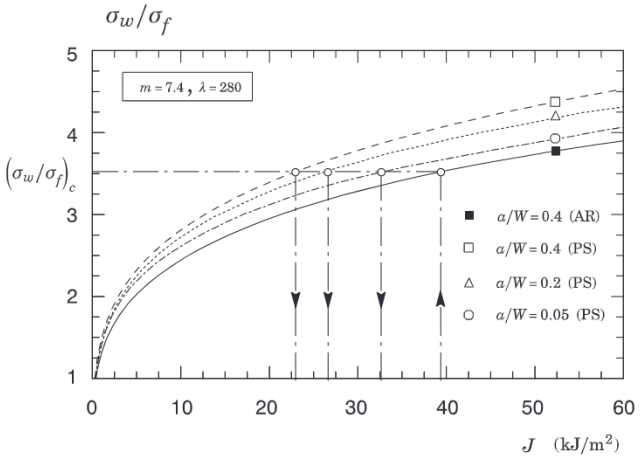

Fig. 11. Constraint correlations of J-values between the as-received deeply-cracked specimen and pre-strain geometries based on the non-dimensional Weibull stress, $\bar{\sigma}_w$.

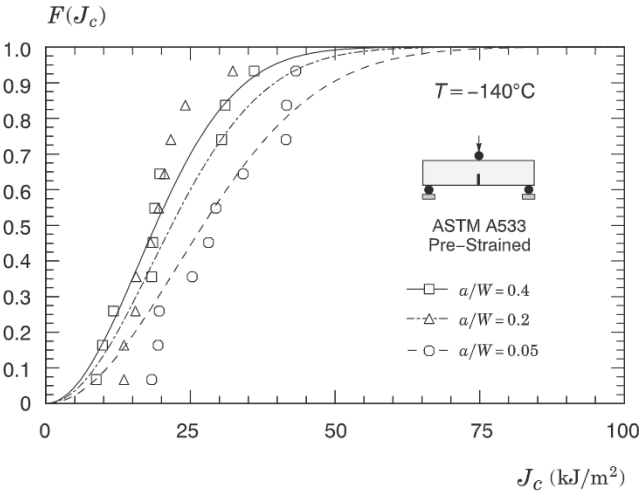

Fig. 12. Predicted cumulative Weibull distribution of experimentally measured J_c-values for the pre-strained SEN(B) specimens using the toughness distribution for the deeply-cracked SEN(B) specimen in the as-received condition.

σ_w-methodology. Note that J_c-values are now plotted on a different scale to highlight the constraint differences between the deep and shallow crack specimens. The lines in these plots represent the prediction of the median fracture probability corresponding to the two-parameter Weibull distribution for J_c-values using the predicted values of characteristic toughness with $\alpha = 2$, refer to previous Eq. (13). The predicted distributions for the specimens with $a/W = 0.4$ and $a/W = 0.05$ are in very good agreement with the experimental data.

Now direct attention to the predicted Weibull distribution for the specimen with $a/W = 0.2$. Here, the predicted Weibull cumulative distribution is almost entirely shifted slightly to the right of the experimental data, thereby providing somewhat non-conservative estimates of fracture toughness values for this specimen configuration. From the results for characteristic toughness given in Table 3, it is seen that the experimental data for the pre-strained material leads to $J_0^{a/W=0.2} > J_0^{a/W=0.4}$, which is not an expected outcome. One possibility is to attribute this outcome to the insufficient number of experimental fracture toughness data points, leading to insufficiently accurate estimation of one or both characteristic toughness values for the pre-strained material. Nevertheless, improved estimates using more data points are not likely to shift significantly the values shown in Table 3, albeit it could provide $J_0^{a/W=0.2} < J_0^{a/W=0.4}$. It is likely that the two values will remain close, for example similar to the predictions based on the

σ_w-methodology shown in the last column of Table 3. The good predictions of the proposed methodology for the specimens with $a/W = 0.4$ and $a/W = 0.05$ lend support to such a suggestion.

Considering the results across the three constraint conditions of as-received and pre-strained material suggests coupling between pre-straining (change of initial conditions) and constraint (change of triaxiality). The change of initial conditions "washes-out" the beneficial effect of lower triaxiality and brings closer the characteristic fracture toughness values of geometries with different triaxilities.

The scaling procedure with non-dimensional Weibull stress appears to be appropriate for predicting changes of fracture toughness due to changed initial conditions as a result of pre-straining. This suggests that predictions for pre-strained material can be made using fracture toughness data from the original material and simple tensile test results from the pre-strained material. This approach could potentially be extended for predicting toughness evolution for given load history – an extension that would require substantial testing for validation. There is no guarantee, however, that a similar approach based on non-dimensional Weibull stress can be applied to cases where changes of flow properties result from a different physical process, most notably changes in temperature. The temperature effect on flow properties arises from rising or lowering critical shear stresses on available crystallographic slip planes, while pre-straining effect on flow properties is of a different nature as discussed in Section 2.

6. Conclusions

This work presents a local approach to describe the effects of constraint loss and pre-strain on macroscopic changes in cleavage fracture toughness applicable to fracture specimens tested in the ductile-to-brittle transition region. The approach builds upon the Weibull stress concept incorporating the statistics of micro-cracks, plastic strain effects, and the influence of pre-strain on the number of eligible micro-cracks nucleated from brittle particles. Through appropriate calibration, the potentially strong variations in crack front stress and strain fields due to the effects of constraint loss are captured. The study described here supports the following conclusions:

- Pre-straining, which can be considered as a proxy for load history effects, results in changes of both the microscopic elastic and flow properties, which are caused by early dislocation mobility and possibly generation of micro-cracks. This in turn affects the initial conditions for calculating the Weibull stress, interpreted as the local approach crack driving force. The pre-straining applied here is shown to wash-out significantly the benefit of lower constraint in providing higher apparent fracture toughness.
- The calibration procedure, which uses a two-step strategy to identify the Weibull parameters m and λ, is well suited for robust assessments of constraint and pre-strain effects on macroscopic measures of fracture toughness, provided two sets of test specimens exhibiting largely contrasting toughness behaviour are available. Calibrations with data obtained with small constraint differences may not provide accurate predictions for constraint conditions outside the calibration interval.
- The Weibull stress model, incorporating a relatively simple modification to take into account the density of eligible micro-cracks based on an exponential distribution, provides good prediction results of the characteristic toughness, J_0, and, consequently, the toughness distributions for the tested material in both as-received and pre-strain conditions. In particular, the toughness distributions for the pre-strain fracture specimens estimated from the measured fracture toughness for the as-received deeply-cracked bend geometry in good agreement with the experimental measurements.
- The study suggests that fracture testing of a deep and shallow crack specimen in the as-received condition, required for accurate model calibration, and tensile testing of a pre-strain material is sufficient to obtain good predictions of pre-strain effects on cleavage fracture toughness. This point could be generalised to more complex load history cases with further experimentation and analysis along the lines presented in the work.

Declaration of Competing Interest

No conflict of interest exists with any party.

Acknowledgments

Jivkov and Ruggieri acknowledge the financial support of the Royal Academy of Engineering, UK, through the Newton Research Collaborative Program Grant NRCP1617/6/19, signed between University of Manchester (UK) and University of São Paulo (Brazil). Further, Ruggieri and Jivkov acknowledge gratefully the support of FAPESP and the University of Manchester, respectively, via the SPRINT exchange programme. Beswick acknowledges the support of EPSRC and Wood via the Nuclear Engineering Doctorate (EngD) Training Centre, grant EP/G037426/1, for the experimental part of the work. In addition, Jivkov acknowledges gratefully the financial support of EPSRC via grant EP/N026136/1.

Appendix A. Experimental data from fracture toughness tests

The data in this appendix is obtained with SEN(B) specimens of A533B with standard dimensions – thickness $B = 25$ mm; width $W = 50$ mm, span S = 200 mm, and three different crack lengths: $a/W = 0.4$ in Table A1; $a/W = 0.2$ in Table A2; and $a/W = 0.05$ in Table A3. Each table includes data, measured or calculated, for as-received and pre-strained material conditions. The tables show experimentally measured initial crack

Table A1
SEN(B) specimens with $a/W = 0.4$.

Specimens of as-received material						Specimens of pre-strained material					
ID	a_0	F_c	d_c	J_c	M	ID	a_0	F_c	d_c	J_c	M
DC4C	20.738	66.59	0.299	44.9	391	DC12P	20.685	43.70	0.183	19.7	595
DC1C	20.561	64.45	0.273	40.4	437	DC1A2P	20.529	34.66	0.138	11.7	1008
DC1D	20.712	68.83	0.301	48.0	366	DC22P	20.718	52.85	0.231	31.0	378
DC2B	20.785	67.56	0.289	46.1	380	DC2A2P	20.530	53.32	0.231	30.4	388
DC2D	20.683	73.86	0.325	55.4	317	DC32P	20.754	42.66	0.178	18.8	622
DC3D	20.588	32.08	0.125	9.7	1819	DC3A2P	20.736	42.58	0.178	18.5	633
DC3C	20.786	63.55	0.269	39.3	446	DC42P	20.533	30.64	0.123	8.7	1355
DC5D	20.711	54.78	0.227	28.8	610	DC4A2P	20.830	56.22	0.257	36.0	324
DC4D	20.442	57.80	0.232	31.9	556	DC52P	20.640	42.35	0.186	18.3	642
DC5C	19.913	51.32	0.205	25.0	722	DC5A2P	20.570	31.77	0.137	9.8	1201

Table A2
SEN(B) specimens with $a/W = 0.2$.

Specimens of as-received material						Specimens of pre-strained material					
ID	a_0	F_c	d_c	J_c	M	ID	a_0	F_c	d_c	J_c	M
DC1A	10.754	125.03	0.192	56.9	413	DC11P	10.714	66.47	0.102	15.6	1007
DC4A	10.205	108.40	0.143	41.0	582	DC1A1P	10.668	70.64	0.109	18.1	869
DC1B	10.688	128.80	0.203	61.9	381	DC21P	10.689	74.91	0.114	20.5	767
DC2A	10.935	136.33	0.229	75.5	310	DC2A1P	10.631	62.00	0.097	13.5	1166
DC2C	10.535	86.95	0.121	25.5	929	DC31P	10.581	92.51	0.149	32.3	488
DC5B	10.550	71.93	0.100	16.7	1417	DC3A1P	10.717	65.66	0.100	13.5	1164
DC4B	10.474	116.34	0.173	47.5	499	DC41P	10.622	77.32	0.121	21.6	729
DC5A	10.630	87.85	0.127	25.7	919	DC4A1P	10.621	74.08	0.114	19.5	808
DC3A	10.716	115.05	0.169	50.8	464	DC51P	10.577	67.11	0.100	15.5	1017
DC3B	10.449	101.02	0.150	38.1	623	DC5A1P	10.688	80.49	0.127	24.1	652

Table A3
SEN(B) specimens with $a/W = 0.05$.

Specimens of as-received material						Specimens of pre-strained material					
ID	a_0	F_c	d_c	J_c	M	ID	a_0	F_c	d_c	J_c	M
SC1A	2.300	130.38	0.063	19.3	1483	SC1A2P	2.601	146.26	0.082	28.1	675
SC1C	2.592	154.53	0.076	25.2	1129	SC12P	2.681	142.97	0.078	25.3	748
SC2A	–	–	–	–	–	SC2A2P	2.660	130.70	0.071	19.6	966
SC2C	2.609	199.11	0.159	81.5	349	SC22P	2.662	158.56	0.093	34.1	555
SC3A	2.882	226.50	0.205	112.6	251	SC3A2P	2.679	168.81	0.105	41.6	455
SC3C	2.765	215.38	0.164	86.37	328	SC32P	2.578	151.85	0.084	29.4	645
SC4A	2.749	219.58	0.175	92.9	305	SC4A2P	2.591	174.11	0.109	43.2	439
SC4C	2.632	209.23	0.145	73.5	387	SC42P	2.532	170.73	0.104	41.5	458
SC5A	2.426	98.75	0.183	98.8	289	SC5A2P	2.649	127.17	0.068	19.4	976
SC5C	2.760	81.33	0.160	81.3	349	SC52P	2.677	126.39	0.066	18.3	1034

lengths, a_0 in mm, loads at fracture, F_c in kN, and crack mouth opening displacements at failure, d_c in mm, together with the fracture toughness values, J_c in kJ/m^2, calculated by ASTM 1921 [21] from the load-CMOD records, and the deformation limits, $M = (W - a_0)\sigma_0/J_c$ (proportionality stress is used for consistency with the main text; the use of the proof stress would increase the deformation limits even further).

Appendix B. Supplementary material

Supplementary data to this article can be found online at https://doi.org/10.1016/j.tafmec.2019.102380.

References

[1] F. Masuyama, History of power plants and progress in heat resistant steels, ISIJ Inter. 41 (2001) 612–625.
[2] J. Knott, Brittle fracture in structural steels: perspectives at different size-scales, Philos. Trans. Royal Soc. A 373 (2015) 20140126.
[3] G.E. Lucas, An evolution of understanding of reactor presser vessel steel equipment, J. Nucl. Mater. 407 (2010) 59–69.
[4] T. Michler, J. Naumann, Microstructural aspects upon hydrogen environment embrittlement of various bcc steels, Int. J. Hydrogen Energy 35 (2010) 821–832.
[5] A. Mirzaee-Sisan, C.E. Truman, D.J. Smith, M.C. Smith, Interaction of residual stress with mechanical loading in a ferritic steel, Eng. Fract. Mech. 74 (2007) 2864–2880.
[6] S.R. Bordet, B. Tanguy, J. Besson, S. Bugat, D. Moinereau, A. Pineau, Cleavage fracture of RPV steel following warm pre-stressing: micromechanical analysis and interpretation through a new model, Fatigue Fract. Eng. Mater. Struct. 29 (2006) 799–816.
[7] A. Pineau, B. Tanguy, Advances in cleavage fracture modelling in steels: Micromechanical, numerical and multiscale aspects, Comp. Rend. Phys. 11 (2010) 316–325.
[8] D.A. Curry, Cleavage micromechanisms of crack extension in steels, Metal Sci. 14 (1980) 319–326.
[9] K. Wallin, The scatter in KIc results, Eng. Fract. Mech. 19 (1984) 1085–1093.
[10] F.M. Beremin, A local criterion for cleavage fracture of a nuclear pressure vessel steel, Metal. Trans. A 14 (1983) 2277–2287.
[11] P.M. James, M. Ford, A.P. Jivkov, A novel particle failure criterion for cleavage fracture modelling allowing measured brittle particle distributions, Eng. Fract. Mech. 121–122 (2014) 98–115.
[12] C. Ruggieri, A.P. Jivkov, A local approach to cleavage fracture incorporating the measured statistics of microcracks, in: Proc. 6th Int. Conf. Crack Paths, Verona, Italy, 19–21 September 2018.
[13] C.J. McMahon Jr., M. Cohen, Initiation of cleavage in polycrystalline iron, Acta Metal. 13 (1965) 591–604.
[14] J. Gurland, Observations on the fracture of cementite particles in a spheroidized 1.05% C steel deformed at room temperature, Acta Metal. 20 (1972) 735–741.
[15] C. Ruggieri, R.H. Dodds Jr., A local approach to cleavage fracture modelling: an overview of progress and challenges for engineering applications, Eng. Fract. Mech. 187 (2018) 381–403.
[16] C. Ruggieri, R. Savioli, R.H. Dodds Jr., An engineering methodology for constraint corrections of elastic-plastic fracture toughness – Part II: effects of specimen geometry and plastic strain on cleavage fracture predictions, Eng. Fract. Mech. 146 (2015) 185–209.
[17] D.F.B. Sarzosa, R.G. Savioli, C. Ruggieri, A.P. Jivkov, J. Beswick, A local approach to assess effects of specimen geometry on cleavage fracture toughness in reactor pressure vessel steels, in: Proc. ASME 2018 PVP Conf., July 15–20, 2018, Prague, Czech Republic.
[18] G.T. Hahn, The influence of microstructure of brittle fracture toughness, Metal. Trans. A 15A (1984) 947–959.
[19] BS7448 Part I. Fracture mechanics toughness tests: Method for determination of KIC, critical CTOD and critical J values of metallic materials, British Standards Institute, 1997.
[20] BS EN 10002-5: Tensile Testing of Metallic Materials, British Standards Institute, 1992.
[21] E1921: Standard Test Method for Determination of Reference Temperature, T0, for Ferritic Steels in the Transition Range, ASTM International, 2017.
[22] N.R. Mann, R.E. Schafer, N.D. Singpurwalla, Methods for Statistical Analysis of Reliability and Life Data, John Wiley & Sons, New York, 1974.
[23] F. Minami, A. Brückner-Foit, D. Munz, B. Trolldenier, Estimation procedure for the Weibull parameters used in the local approach, Int. J. Fract. 54 (1992) 197–210.
[24] J.A. Benito, J.M. Manero, J. Jorba, A. Roca, Change in Young's modulus of cold- deformed pure iron in a tensile test, Metal. Mater. Trans. 36A (2005) 3317–3324.
[25] M. Yang, Y. Akiyama, T. Sasaki, Evaluation in change in material properties due to plastic deformation, J. Mater. Proc. Tech. 151 (2004) 232–236.
[26] Z. Chen, U. Gandhi, J. Lee, R.H. Wagoner, Variation and consistencies in Young's modulus of steel, J. Mater. Proc. Tech. 227 (2016) 227–243.
[27] ABAQUS Documentation, © Dassault Systèmes, 2015, Providence, RI, USA.
[28] C. Shih, B. Moran, T. Nakamura, Energy release rate along a three-dimensional crack front in a thermally stressed body, Int. J. Fract. 30 (1986) 79–102.
[29] C. Ruggieri, R.H. Dodds, A transferability model for brittle fracture including constraint and ductile tearing effects: a probabilistic approach, Int. J. Fract. 79 (1996) 309–340.
[30] X. Gao, C. Ruggieri, R. Dodds, Calibration of Weibull stress parameters using fracture toughness data, Int. J. Fract. 92 (1998) 175–200.